Strong-field effects in the photo-emission spectrum of the C_{60} fullerene

C.-Z. Gao,[1,2] P. M. Dinh,[1,2] P. Klüpfel,[3] C. Meier,[3] P.-G. Reinhard,[4] and E. Suraud[1,2]

[1] *Université de Toulouse; UPS; Laboratoire de Physique Théorique, IRSAMC; F-31062 Toulouse Cedex, France*
[2] *CNRS; UMR5152; F-31062 Toulouse Cedex, France*
[3] *Université de Toulouse; UPS; Laboratoire Collisions-Agrégats-Réactivité, IRSAMC; F-31062 Toulouse Cedex, France*
[4] *Institut für Theoretische Physik, Universität Erlangen, Staudtstraße 7, D-91058 Erlangen, Germany*

(Dated: draft, January 15, 2016)

Considering C_{60} as a model system for describing field emission from the extremity of a carbon nanotip, we explore electron emission from this fullerene excited by an intense, near-infrared, few-cycle laser pulse (10^{13}-10^{14} W/cm^2, 912 nm, 8-cycle). To this end, we use time-dependent density functional theory augmented by a self-interaction correction. The ionic background of C_{60} is described by a soft jellium model. Particular attention is paid to the high energy electrons. Comparing the spectra at different emission angles, we find that, as a major result of this study, the photoelectrons are strongly peaked along the laser polarization axis forming a highly collimated electron beam in the forward direction, especially for the high energy electrons. Moreover, the high-energy plateau cut-off found in the simulations agrees well with estimates from the classical three-step model. We also investigate the build-up of the high-energy part of a photoelectron spectrum by a time-resolved analysis. In particular, the modulation on the plateau can be interpreted as contributions from intracycle and intercycle interferences.

arXiv:1601.03606v1 [physics.atm-clus] 14 Jan 2016

I. INTRODUCTION

Emission from nanometric tips subject to possibly intense laser fields is of strong current interest as it constitutes a promising source of a well collimated and coherent beam of ultrafast electrons [1], which can be used in electron diffraction experiments [2] as well as electron microscopy [3]. Such systems could be especially interesting in the recollision regime (in which emitted electrons recollide with the tip in the course of the laser pulse) as this could allow to generate extremely short electron pulses [4] and thus pave the way to sub-femtosecond and sub-nanometric probing of matter [5]. Most studies have up to now focused on metallic nanotips. In particular, laser-induced photo-emission of electrons in the recollision regime, manifesting itself in the formation of a plateau at high kinetic energies in the photo-electron spectrum (PES), has been very recently observed in tungsten tips of nanometric size [6–8]. In this context, carbon nanotubes have also been proposed as promising emitting devices, since they possess an even smaller tip size than the metal tips used so far [9]. These novel structures have mainly been characterized by field emission experiments [10, 11]. Due to this smaller tip size of carbon nanotubes, these systems might thus lead to even more promising sources for sub-femtosecond / sub-nanometric probing of dynamic processes in various areas of physics, chemistry, biochemistry or material science. Only very recently, laser-assisted photo-electron studies, which have been very successful in the case of metal nanotips, have been extended to these novel tips based on carbon nanostructures [12].

In relation to this question of field emission from carbon nanotips, the present work aims at studying to which extent photo-emission by ultrafast laser pulses can reach the intended recollision regime in carbon nanostructures. As a starting point, we shall focus our analysis on the actual extremity of the tip which practically consists in the cap of a nanotube (the tip is formed by rolling graphene sheets with various radii and helical structures). The cap of the carbon nanotubes used in the above mentioned photo-emission experiments are similar in size and structure to a C_{60} cluster [13]. In this first step we shall thus use C_{60} as a test model for the exploratory studies presented here. We consider the response of C_{60} subject to an intense laser irradiation and characterize this response in terms of photo-electron spectra (PES).

The paper is outlined as follows: Section II briefly introduces the theoretical framework and computational details. Section III presents and discusses the results. Section IV completes the paper with a conclusion.

II. FORMAL FRAMEWORK

A. Time-dependent local-density approximation

We describe electron dynamics by means of time-dependent density-functional theory at the level of the time-dependent local-density approximation (TDLDA). The LDA is complemented by an average-density self-interaction correction (SIC), which has been shown to provide a reliable theoretical framework of electron dynamics in strong laser fields, in particular when the excitation leads to substantial ionization [14, 15]. The detailed theoretical approach is given elsewhere, and shall only briefly be summarized here. The time-dependent single-particle (s.p.) wave functions $\varphi_j(\mathbf{r},t)$ are obtained by solving the time-dependent Kohn-Sham equations [16] (here and in the following we use atomic units) :

$$\mathrm{i}\frac{\partial}{\partial t}\varphi_j(\mathbf{r},t) = \{-\frac{1}{2}\nabla^2 + \upsilon_{\mathrm{C}}[\rho(\mathbf{r},t)]$$

$$+ v_{\rm xc}[\rho(\mathbf{r},t)] + v_{\rm ext}(\mathbf{r},t)\}\varphi_j(\mathbf{r},t), \quad (1a)$$

$$v_{\rm ext} = v_{\rm jel} + v_{\rm las}, \quad (1b)$$

where $v_{\rm C}$ is the standard Coulomb potential and $v_{\rm xc}$ the exchange-correlation potential from DFT [17] using the exchange-functional given in [18]. This potential depends on the actual electron density

$$\rho(\mathbf{r},t) = \sum_{j=1}^{N_{\rm el}} |\varphi_j(\mathbf{r},t)|^2. \quad (2)$$

where $N_{\rm el}$ is the number of electrons. The external one-body potential $v_{\rm ext}$ is composed from the potential of the ionic background potential, here modeled as a jellium (see section II B), and the potential of the laser field (see section II C).

B. Ionic background

The positively charged ionic background is approximated by a jellium model. Specifically for C_{60} considered here, all carbon ions are arranged into a shell-like structure [19]. The model for the jellium potential $v_{\rm jel}$ for the ionic background reads :

$$v_{\rm jel}(\mathbf{r}) = -\int \mathrm{d}^3\mathbf{r}' \frac{\rho_{\rm jel}(|\mathbf{r}'|)}{|\mathbf{r}-\mathbf{r}'|} + v_{\rm ps}(|\mathbf{r}|)\ , \quad (3a)$$

$$\rho_{\rm jel}(r) = \rho_0\, g(r)\ , \quad (3b)$$

$$v_{\rm ps}(r) = v_0\, g(r)\ , \quad (3c)$$

$$g(r) = \frac{1}{1+\exp\left[(r-R_-)/\sigma\right]}\ \frac{1}{1+\exp\left[(R_+-r)/\sigma\right]} \quad (3d)$$

$$R_\pm = R \pm \frac{\Delta R}{2}\ . \quad (3e)$$

The jellium density $\rho_{\rm jel}$ is modeled by a sphere of positive charge with a void at the center [20–22]. The Woods-Saxon profile g generates a transition from bulk shell to the vacuum (inside and outside), providing soft surfaces. Furthermore, we employ a pseudo-potential $v_{\rm ps}$ in addition to the potential created by the jellium density, as proposed in Ref. [23], which is tuned to ensure reasonable values of the single-particle energies. The average radius R of the jellium cage is taken from experimental data as $R = 6.7$ a$_0$ [24]. The thickness of the jellium shell ΔR, the surface softness σ, and the depth of the potential well v_0 are adjustable parameters for which we use here $\sigma = 0.6$ a$_0$, $v_0 = 1.9$ Ry, and $\Delta R = 2.57$ a$_0$. The bulk density ρ_0 is determined such that $\int \mathrm{d}^3\mathbf{r}\,\rho_{\rm jel}(\mathbf{r}) = N_{\rm el} = 238$. Note that this number of electrons is different from 240 for a real C_{60}, but no jellium model is capable to place the electronic shell closure at this value so far (unless one uses a deliberate modification of the occupation numbers [25]). Most jellium models for C_{60} have the shell closure at $N_{\rm el} = 250$ [20–22]. The present model with soft surfaces comes to $N_{\rm el} = 238$ which is much closer to reality. By virtue of the choice of model parameters, the electronic properties of C_{60} are well reproduced, in particular the ionization potential (IP) at $E_{\rm IP} = 0.56$ Ry, that is identical to the experimental value [26], a HOMO-LUMO gap of 0.14 Ry, which is well within the range of the experimental values (0.12-0.15 Ry [27]), as well as a good description of the photo-absorption spectrum (for details, see [23]).

The use of the jellium approximation, nevertheless, requires some words of caution. The standard procedure is to use a detailed ionic background coupled to the electrons through pseudo-potentials. There exist numerous investigations for C_{60} [28, 29] and other carbon nanostructures such as graphene [30] or nanotubes [31]. An elaborate description of C_{60} with an involved orientation averaging is needed for detailed observables such as photo-electron spectra (PES) and photo-angular distributions (PAD) [32–34]. A key issue in the present investigations is the ponderomotive motion of the electron in the laser field associated with huge excursions of the electron [35]. This requires extremely large simulation boxes which become unaffordable for a grid representation in full 3D. The jellium model, together with the linearly polarized laser field, has cylindrical symmetry. This allows us to use a cylindrical (2 dimensional) box which renders the necessary huge boxes feasible. As an additional benefit, we can also compute angular distributions without the extra expense of orientation averaging [36, 37]. As far as the jellium model is concerned, it is a powerful approximation as it provides an appropriate description of many features of the electronic structure and dynamics in solids [38], cluster physics [39, 40], and C_{60} [21]. However, two aspects have been sacrificed. The first one is that the returning electron collides with the jellium well instead of with a carbon ion. Although the potential of the ionic background is very steep, we are probably underestimating the actual yield of high-energy electrons. The second aspect is that we ignore ionic motion. As a consequence, we miss effects from phonon coupling [41] as well as from electronic dissipation [42]. However, since we are using femtosecond laser pulses, their effect should not drastically affect the main findings presented here.

C. Laser field

The laser field is taken to be linearly polarized along the z direction, with a $\sin^2$-shaped envelope,

$$\mathbf{E}_{\rm las}(t) = E_0 \sin^2\left(\pi t/T_{\rm pulse}\right) \sin(\omega_{\rm las} t + \phi_{\rm CEP})\, \mathbf{e}_z\ . \quad (4)$$

Within the dipole approximation in length gauge, the laser-electron interaction is given by $V_{\rm las}(\mathbf{r},t) = -\mathbf{E}_{\rm las}(t)\cdot\mathbf{r}$. We use a laser frequency $\omega_{\rm las}$=1.36 eV (=912 nm) and a total duration $T_{\rm pulse} = 24$ fs. The laser strength E_0 is varied from 0.0113 V/a$_0$ to 0.0453 V/a$_0$, corresponding to laser intensities $I_{\rm las}$ from 10^{13} W/cm^2 to 1.6×10^{14} W/cm^2. It is instructive to characterize these laser conditions in terms of the Keldysh parameter $\gamma = \sqrt{2E_{\rm IP}}\,\omega_{\rm las}/E_0$ where $E_{\rm IP}$ is the ionization potential [43]. The current combination of $\omega_{\rm las}$ and E_0

spans the interval $0.55 \leq \gamma \leq 2.2$, i.e., from multi-photon ionization for $\gamma > 1$ to tunneling ionization for $\gamma < 1$. This transition has been experimentally studied in PES of rare gases [44]. In the above expression, $\phi_{\rm CEP}$ is the carrier-envelope phase (CEP). A recent combined experimental/theoretical study on strong-field ionization in C_{60} [45] reported a remarkable CEP effect. In these studies, a pulse duration of 4 fs and a central frequency of $\omega_{\rm las} = 1.72$ eV have been used. However, in the present work, much longer pulses (of about 8 optical cycles) are used. We have performed a systematic analysis by varying the CEP and found no significant influence on the PES. As a consequence, only results for $\phi_{\rm CEP} = 0$ are shown below.

D. Numerical representation

A detailed description of the numerical treatment can be found in [46, 47]. Here, we give a brief account and specify the actual numerical parameters used. Wave functions, densities, and fields are represented on a cylindrical grid in coordinate space. As already mentioned, a major issue of the present investigation is the rescattering of electrons which requires very large computational boxes for a complete description of the huge electron excursions. We have thus made systematic investigations on the impact of box parameters. The final choice is a compromise between acceptable numerical cost, accuracy and robustness. The chosen dimensions of the numerical box are 500 a_0 along the laser polarization direction (z axis) and 250 a_0 in radial direction (r coordinate). The grid spacing is taken to be 0.5 a_0, which allows us to represent kinetic energies up ∼140 eV. The electronic ground state is determined by the damped gradient method [48]. The Kohn-Sham wave functions are propagated in time using the time-splitting technique [49], and absorbing boundary conditions are used to remove all (emitted) electrons which have reached the boundaries of the box. They consist of 70 grid points (=35 a_0) at each of the margins.

E. Observables

We have studied various observables related to the response of the system, in particular to ionization. The total ionization is calculated as the difference between the initial number of electrons $N_{\rm el}$ and those left in the box at a given time t :

$$N_{\rm esc}(t) = N_{\rm el} - \int {\rm d}^3\mathbf{r}\, \rho(\mathbf{r},t). \qquad (5)$$

This quantity gives an indication on the charge state of C_{60} after irradiation [15]. Another observable is the electronic dipole moment

$$\mathbf{D}(t) = \int {\rm d}^3\mathbf{r}\, \rho(\mathbf{r},t)\, \mathbf{r}, \qquad (6)$$

which characterizes the electronic response in time. It is mostly used to compute photo-absorption spectra using spectral analysis [50]. Here we use it in the time domain to visualize the electron dynamics of the system. In the following, we will consider particularly the dipole moment parallel to the laser polarization, that is D_z.

Most importantly, we will concentrate our analysis of electron emission on the angular-resolved photo-electron spectra (ARPES) yield $\mathcal{Y}(E_{\rm kin},\theta)$, that is the yield of asymptotic kinetic energies $E_{\rm kin}$ of electrons emitted in direction of angle θ. To evaluate $\mathcal{Y}$ from our TDDFT simulations, we employ the method initiated in [51, 52] and extended in [53] to the case of strong fields as used here. In brief, the PES is computed by recording the single-particle wave functions $\psi_j(t,\mathbf{r}_\mathcal{M})$, $j = 1,\ldots,N_{\rm el}$, at selected sampling points $\mathbf{r}_\mathcal{M}$ near the absorbing boundary. Once the simulation is completed, one computes the Fourier transform from time to frequency domain $\widetilde{\psi_j}(E_{\rm kin},\mathbf{r}_\mathcal{M})$ augmented by a phase factor accounting for the external field [53]. The PES then reads

$$\mathcal{Y}(E_{\rm kin},\theta) \propto \sum_{j=1}^{N_{\rm el}} |\widetilde{\psi_j}(E_{\rm kin},\mathbf{r}_\mathcal{M})|^2 \quad . \qquad (7)$$

The sampling points are chosen to cover a mesh of emission angles θ. This angle θ at detection point $\mathbf{r}_\mathcal{M}$ is defined with respect to the laser polarization $\mathbf{e}_z$: forward and backward emissions correspond to $\theta = 0°$ and $\theta = 180°$ respectively. The energy and angle resolution for the PES is 0.04 eV and 1° respectively.

III. RESULTS AND DISCUSSIONS

A. Angular dependence of the photoelectron spectra

The upper panel of Fig. 1 shows the full ARPES at intensity $I_{\rm las} = 1.6 \times 10^{14}$ W/cm^2 complemented by the angular distribution (PAD) on the right. This PAD is obtained from integration of the ARPES over the kinetic energy interval 50–160 eV, while the lower panel shows the PES for selected angles, as indicated. The ARPES clearly indicates that electron emission is more pronounced for higher energies and is strongly focused in forward direction ($\theta = 0°$) : The ratio of the yield at 0° and at 90° increases from ∼ 100 at low energies to ∼ 10^5 in the high energy range (100–150 eV). Analyzing the angular distributions in Fig. 1 (b) yields a focusing of ∼ 7° (full width at half maximum), similar to values observed in gold nanotips [54].

In Fig. 1(c), we present the photoelectron spectra for different emission angles, as indicated. All four PES start with a nearly exponential decrease and then, for higher energies, develop into a broad plateau which extends up to a distinct cut-off. We will discuss this structure in more details in the next section. Note that this typical pattern is well known and can be qualitatively un-

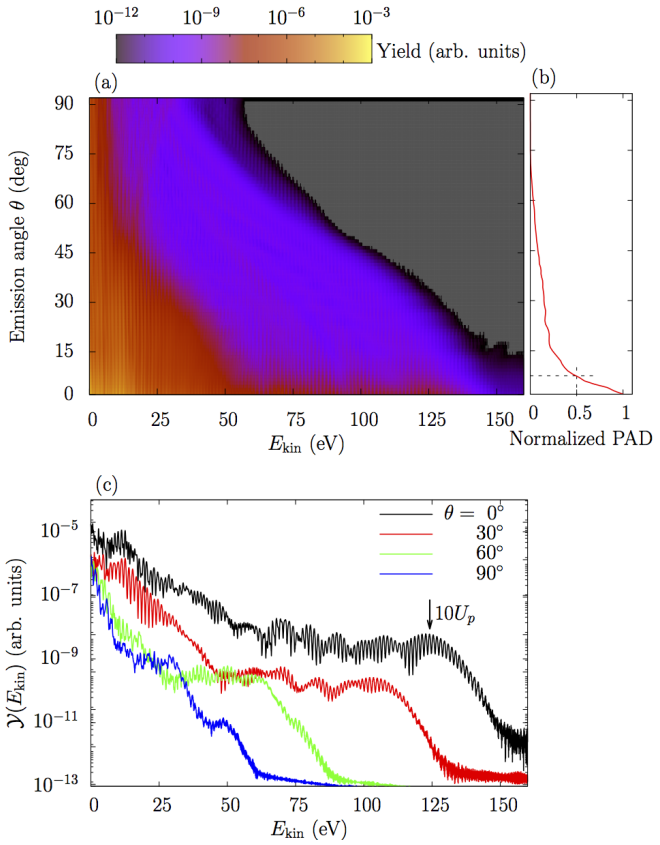

Figure 1. (a): Color map of angle-resolved photo-electron spectra (ARPES) as a function of kinetic energy and emission angle, in logarithmic scale for the yield, from C_{60} excited by a laser pulse with following parameters : $\omega_{las} = 1.36$ eV, $T_{pulse} = 24$ fs, $I_{las} = 1.6 \times 10^{14}$ W/cm^2. (b): PAD obtained from integration of the ARPES over the high-energy range of [50–160 eV], normalized to 1 at 0°. The dashed line marks the cone angle at full width at half maximum. (c): PES for emission angles at $\theta = 0°, 30°, 60°,$ and 90° (in logarithmic scale), with an arrow indicating the $10U_p$ cutoff energy.

derstood by the so called "three-step model" [55]: the electron is ionized during the laser field through tunnel ionization, then accelerated in the electric field, driven back to the ion core and gains a large amount of energy through recollision with the latter. Within this simple picture, the cut-off appears at $\sim 10U_p$ with $U_p = \frac{I_{las}}{4\,\omega_{las}^2}$ being the ponderomotive energy. Here, the angular dependence of the cut-off roughly follows a $\cos\theta$ dependence, similar to the angular tendency of cut-off shown in [56, 57]. A further interesting finding is the oscillatory structure of the PES within the high energy plateau. Similar structures have been observed in other systems [58, 59], where they were interpreted as interference effects of different electron trajectories leading to the same final kinetic energy. In Sec. C, we will analyze the time evolution of the spectra, and we will show that this interpretation is consistent with our results. In the following section, we will first address the intensity dependence of the photoelectron spectra.

B. Impact of laser intensity

1. *PES as a function of laser intensity*

To study the influence of the laser intensity on PES of irradiated C_{60}, four intensities have been explored, namely I_0, $2I_0$, $4.6I_0$, and $8I_0$ where $I_0 = 2 \times 10^{13}$ W/cm^2, corresponding to values of the Keldysh parameter $\gamma = 1.5$, 1.1, 0.7, and 0.5 respectively. Figure 2 collects the results for the PES in forward direction ($\theta = 0°$). They exhibit similar pattern at all four considered intensities : on the low-energy side, they show a more or less extended plateau (see inset), then turn to a rapid exponential decrease, and finally develop a broad second plateau which extends to high energies. Both plateaus are shifted towards higher kinetic energy with increasing laser intensity, whereby the width of the plateau increases as well and thus the upper energy cut-off of the second plateau increases accordingly.

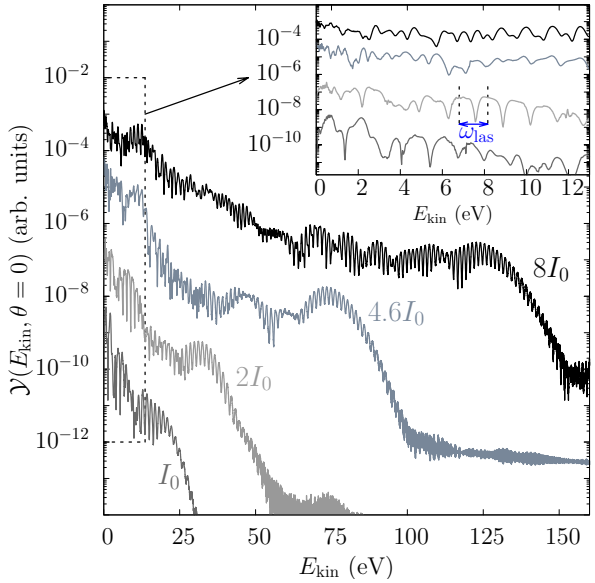

Figure 2. Samples of photo-electron spectra in forward direction in C_{60} irradiated by laser pulses with $\omega_{las} = 1.36$ eV (912 nm), $T_{pulse} = 24$ fs, and four intensities as indicated ($I_0 = 2 \times 10^{13}$ W/cm^2). The curves are vertically shifted for a better graphical discrimination. Inset : zoom in the region $0 < E_{kin} < 13$ eV contributed by direct emissions.

We first concentrate on the PES at low energies ($<$ 13 eV) magnified in the inset of Fig. 2. For the two lowest intensities (I_0 and $2I_0$), they show a dense sequence of peaks which are separated by the photon energy $\omega_{las} = 1.36$ eV. This is the typical pattern for Above-Threshold Ionization (ATI), which has been well studied for C_{60} experimentally [60, 61] and theoretically [32, 33, 62]. These equi-spaced patterns are washed out when the laser in-

tensity increases to the two highest values ($4.6\,I_0$, $8\,I_0$). This can have several reasons: first, due to the significant ionization at these intensities, the cluster progressively becomes charged during the laser pulse, leading to changes in the electronic structure. This effect has been observed in sodium clusters, see e.g. [51, 62], and preliminary investigations have clearly shown similar effects in the present case too. However, additional blurring due to other effects, like the space charge, may also contribute, and will be analyzed in future studies.

2. *Analysis of the high energy plateau*

As mentioned above, the high-energy plateau is generated by strong-field ionization (SFI) mechanism, and the characteristic cut-offs can be found approximately at $10.007\,U_p$ [56]. Moreover, the derivation of a semiclassical cut-off law [63], based on the Strong Field Approximation (SFA), reveals that the IP also plays a role in the SFI regime, and can be estimated by [63]:

$$E_{\rm cut}^{\rm (SFA)} = 10.007\,U_p + 0.538\,E_{\rm IP}\ ,\ U_p = \frac{I_{\rm las}}{4\,\omega_{\rm las}^2}\ , \qquad (8)$$

Because of the inverse quadratic dependence of U_p on the laser frequency $\omega_{\rm las}$, the low value of 1.36 eV used here delivers a large ponderomotive energy and large cut-offs in the PES. For instance, at $4.6I_0$, we have U_p=7.1 eV, largely exceeding the photon energy and being even comparable to $E_{\rm IP}$, and $E_{\rm cut}^{\rm (SFA)} = 75$ eV in Fig. 2.

We have extracted the energy cut-off from our calculated PES, denoted by $E_{\rm cut}^{\rm (TDLDA)}$ to compare it to the simple estimate $E_{\rm cut}^{\rm (SFA)}$ given by Eq. (8). More precisely, for a given PES, $E_{\rm cut}^{\rm (TDLDA)}$ is obtained as the intersect of two fitting exponential curves at each side of the plateau, similarly to the procedure applied on experimental data [64]. The comparison of $E_{\rm cut}^{\rm (TDLDA)}$ and $E_{\rm cut}^{\rm (SFA)}$ is presented in Fig. 3. We first note that both energy cut-offs grow linearly with laser intensity, pointing towards the validity of the simple classical scaling law. However, our numerical simulations show a slightly steeper slope. If one interprets the numerical results obtained by the TDLDA approach in the light of the simple classical scaling law (8), the difference may be explained by a field enhancement of about 5 to 10%. Further investigations are needed to confirm this interpretation. Note however that a similar effect has been observed in metallic nanotips [7, 54, 65].

3. *Ponderomotive oscillations*

To better visualize the ponderomotive motion, we show in the lower panels of Fig. 4 the current density j_z along the laser polarization axis z. Two intensities are considered, one at the moderate side with $I_{\rm las} = I_0 = 2\times10^{13}$ W/cm^2 (left column) and another one at higher intensity of $I_{\rm las} = 4.6\,I_0 = 9.2\times10^{13}$ W/cm^2 (right column). The current density is plotted in a 2D density map as a function of time (horizontal axis) and space coordinate z (vertical axis), with positive j_z in red (or gray) and negative j_z in green (or light gray). It is also instructive to compare these maps with the time evolution of the dipole moment defined in Eq. (6) which is plotted in the top panel of the figure. Note that the dipole moment and the current density are related by the continuity equation which reads :

$$\frac{\partial D_z}{\partial t} = \int_z {\rm d}z\ j_z\ . \qquad (9)$$

The sign of the time derivative of D_z is thus equal to the one of the dominant part of j_z.

One observes successive fringes in j_z connected to the change of sign of the derivative of D_z or, in other words, to the oscillations of D_z in time, as exemplified by vertical dashes in a case when the sign is negative. For the highest laser intensity (right column of Fig. 4), a sizable backflow of the current density occurs during pulse duration, especially between 5 and 15 fs, where the field amplitude is maximal. For instance, in the time interval indicated by the two vertical dashed lines, the majority of electrons possess a negative j_z (they are thus pulled away from the C_{60}), while a non-negligible amount exhibits a positive j_z, which means that they are pulled back towards C_{60} and that recollision is possible. At the lowest $I_{\rm las}$, this backflow still exists but is much weaker, see inset in the bottom left panel for which the current density scale has been divided by 100 to allow the visualization of this weak counterflow. The amplitude of this quiver motion can be estimated from a purely classical model as $l_{\rm q} = \alpha E_0/\omega^2$ where α is the field enhancement factor (here about 1.05). This yields $l_{\rm q} \sim 12$ a$_0$ and ~ 25 a$_0$ at the low and the high $I_{\rm las}$ respectively. These classical

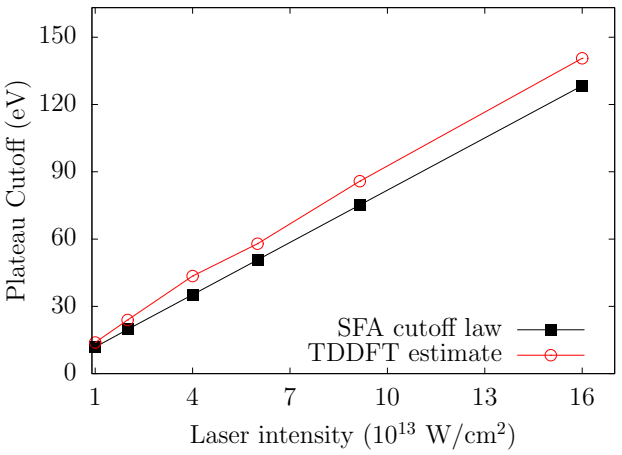

Figure 3. Cutoff energies of the high-energy plateau in the PES as functions of the laser intensity, from TDLDA calculations compared with the estimate (8) deduced from the strong field approximation (SFA).

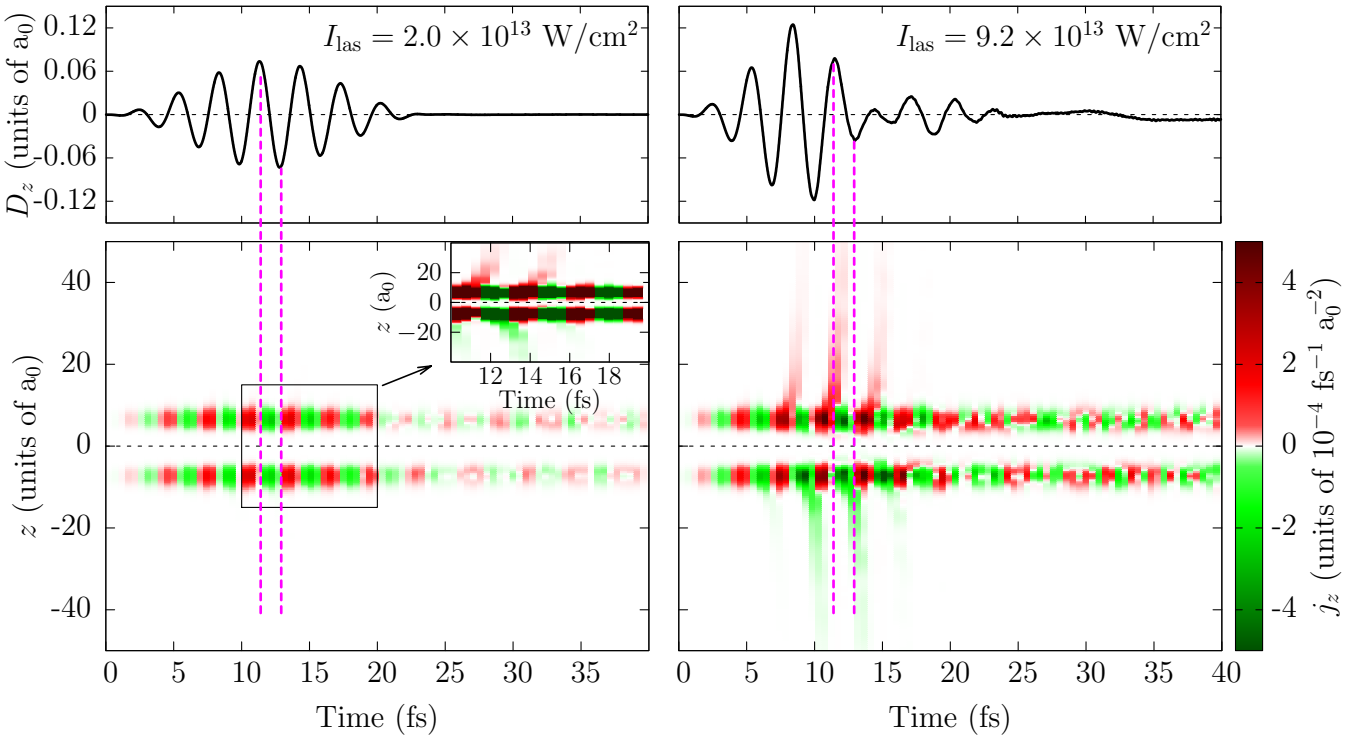

Figure 4. Electronic dipole moment D_z as a function of time (top row), and current density j_z as a function of time and z coordinate (bottom row, 2D density map) of C_{60} along laser polarization axis (z direction), after irradiation by a laser pulse with $\omega_{las} = 1.36$ eV, $T_{pulse} = 24$ fs, and with two different intensities $I_{las} = 2.0 \times 10^{13}$ W/cm^2 (left column) and $I_{las} = 9.2 \times 10^{13}$ W/cm^2 (right column). Positive j_z are depicted in red (or gray), and negative j_z are in green (or light gray). For a given color (or type of gray), the brighter the shade, the smaller the absolute value of j_z. The inset in the left bottom panel magnifies the map between 10 and 20 fs with a scale in current density divided by 100.

l_q agree well with the amplitudes one can read off from the current density maps. The large ponderomotive oscillations terminate as soon as the external field dies out. The further evolution still shows a succession of positive and negative fringes of j_z, but electrons in the $z > 0$ and the $z < 0$ regions do not oscillate in phase anymore. This is particularly visible for the highest I_{las} above 20 fs.

C. Time-resolved analysis

As mentioned above, in addition to the high-energy cut-off, we see modulations of the PES within the broad plateau for the two cases with the higher intensities in Fig. 2. Similar structures have been experimentally observed in the photoemission spectra of rare gases (i.e., argon atom [66]) ionized by strong infrared laser pulses. These structures have been interpreted as interference effects from several electron trajectories generated either in the same optical cycle or in the subsequent optical cycle, leading to the same final states [67]. In particular, in this work, two types of trajectories have been identified, labeled as "short" and "long" trajectories, due to their different excursion times. Within the three-step model, the electrons are born close to the field maxima, where the tunnel ionization probability is maximal.

Since we focus on electron emission in the forward direction, we have chosen, for the time-resolved analysis, instants based on a classical picture of the electron emission. More precisely, the "birth" times of the electrons, denoted by $t_{b1/2/3}$, are taken at the three largest maxima of the electric force, that is at respectively 2.75, 3.75, and 4.75 t_{oc}, where $t_{oc} = 3$ fs is the single optical cycle. We have indicated these birth times in Fig. 5(a). We then correlate $t_{b1/2/3}$ with the detection time $t_{f1/2/3}$. Since the (fastest) electrons generated at t_b need time to reach the boundary where they are detected, we take into account a time delay Δt which consists of two terms. The first one is the "return" time for the electron to recollide with the target and is about $0.75 t_{oc}$. The second one is the time for electrons emitted from the rescattering site to travel to the detection points $R_b = 90$ a$_0$ near the boundary of the simulation box. This "traveling" time is $(R_b - R)/\sqrt{2E_{kin}}$ for electrons recorded with kinetic energy E_{kin}. All in all, we have used :

$$t_f \approx t_b + \Delta t, \tag{10a}$$

$$\Delta t = 0.75 t_{oc} + (R_b - R)/\sqrt{2E_{kin}}. \tag{10b}$$

For t_{b1}, we used $E_{kin} = 70$ eV leading to $\Delta t = 1.04\ t_{oc}$, while for t_{b2} and t_{b3}, we took $E_{kin} = 135$ eV and then

obtained $\Delta t = 0.96\ t_{oc}$. Plugging these numbers in Eqs. (10), we got $t_{f1/2/3} = 3.79$, 4.71, and 5.71 t_{oc} respectively, as symbolized in Fig. 5(b).

The bottom panel of Fig. 5 presents three different PES, note that each one has been analyzed from $t = 0$ up to one of the "final" times introduced above. In addition,

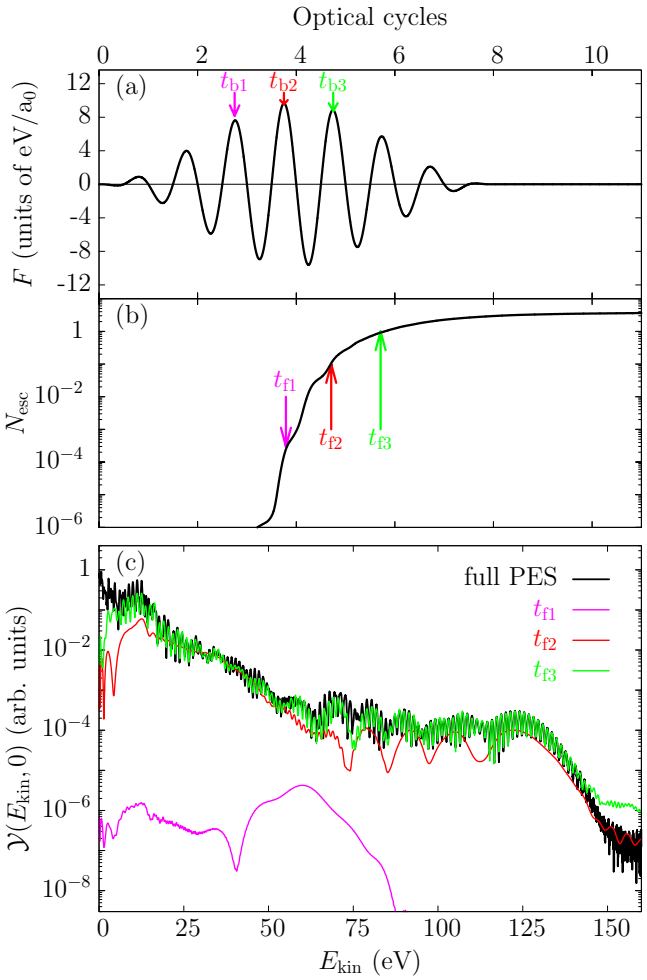

Figure 5. Time-resolved analysis of photo-emission from C_{60} irradiated by a laser pulse polarized in the z direction, with $\omega_{las} = 1.36$ eV, $T_{pulse} = 24$ fs and $I_{las} = 1.6 \times 10^{14}$ W/cm^2. (a) Time evolution of the force F acting on electrons, with 3 "birth" times indicated by arrows (see text for details). (b) Time evolution of the total ionization N_{esc}, with 3 "final" times indicated by arrows and defined in Eqs. (10). (c) Full PES (black) and PES from data accumulated up to the 3 different final times.

the full PES (black curve) obtained at the end of the laser pulse is shown. We can therefore progressively observe how the full PES builds up in time. It should be noted that this analysis is strictly valid only for the high-energy electrons, since low-energy electrons arrive later, and are thus not accounted for at the corresponding final times $t_{f1/2/3}$.

As a first result, we see that the spectra at t_{f1} is about two to three orders of magnitude smaller than the spectra at later times (also see the corresponding ionization in Fig.5(b)), showing that these contributions are negligible. Indeed, at the field maximum indicated by t_{b1}, on the rising part of the pulse envelop, the field strength is not yet sufficient for an efficient tunnel ionization. The major part of the spectrum, containing the main structures, is obtained for the spectrum at t_{f2}, which corresponds to a birth time t_{b2} at the highest field value of the pulse. It shows a clear plateau, with distinct modulations. If one interprets these structures as interferences from two electron trajectories, it would correspond to a relative phase of $\delta S = E_{kin}\delta t$ [68] with δt=0.41 fs, well below the optical period t_{oc}= 3 fs. This value of δt, about one seventh of t_{oc}, is in the same order as deduced by an extended schematic model for recent laser-nanotip interactions, estimated to about one sixth in this case [65]. Within this interpretation of interference of different electron trajectories, the findings of the numerically calculated spectra at t_{f2} would correspond to "intracycle" interferences, i.e., interference that stems from electron trajectories originating during the same optical period. When comparing to the spectrum at t_{f3}, one sees that the additional changes with respect to that at t_{f2} are minor at the side of the extension of the plateau, however, one striking difference can be observed: the appearance of high-frequency modulations in the spectra. These modulations correspond to peaks separated by the central frequency ω_{las}. From a temporal point of view, these structures are created by interferences of electron trajectories that are born at times separated by the optical period, and can thus be identified as "intercycle" interferences. These are commonly observed for longer pulses, where several field peaks have comparable maxima, as it is in the present case.

When compared to the full spectra, one sees slow convergence for the low-energy electrons. This can be understood by the fact that these electrons, due to their slower speed, only arrive at delays much larger than Δt. This systematic effect is clearly visible in all time-resolved spectra.

To summarize, we have analyzed the time evolution of the spectra obtained by the fully numerical TDDFT calculations by choosing particular detection times to separate as fully as possible the contributions from the different field maxima. While not claiming to have unambiguously identified the observed structures, we have shown that their characteristics, both in their time evolution as well as with respect to their frequency fingerprints, are consistent with the picture of interfering intra- and intercycle trajectories.

IV. CONCLUSIONS

In this paper, we have analyzed the electron dynamics of laser-excited C_{60} as a model case for the generation of high-energy electrons from a carbon tip. We have explored the response of the system to laser fields of various

intensities for a frequency in the infrared domain which leads, at high intensities, to significant ponderomotive effects. To analyze such a complex dynamics, we go beyond single-active-electron approaches and use time-dependent density-functional theory propagated in real time and computed on a spatial grid. This approach allows, in particular, a proper description of collective electronic motion as well as a detailed analysis of photo-electron spectra (PES) and photo-angular distributions (PAD). One of the main numerical challenges in the present investigation was the large box size required to account for the huge pathway of the ponderomotive motion of the electrons. To make that feasible in a quantum mechanical framework, we use a spherical jellium approximation for the ionic background and handle the dynamics on a cylindrical grid.

As a major result, we have shown that the recollision regime can be reached for strong, but realistic, laser intensities. We find the establishment of a plateau stretching out to very high kinetic energies, e.g. to about 125 eV for $I = 1.6 \times 10^{14}$ W/cm^2, which is interpreted using the well-known recollision mechanism and illustrated by using a map of the time dependence of the current distribution. The cut-off of the plateau is shown to follow the semiclassical model based on the three-step model, with a field which is enhanced by about 10% in our simulations. A detailed time-resolved analysis of the PES demonstrates how the high-energy plateau is generated successively during the laser pulse. In particular, we have shown that the observed structures and their time evolution stemming from different peaks of the field are consistent with the picture of intra- and intercycle interferences. As far as the angular distribution is concerned, one of the most promising results of the presented study is the strong focusing of the electrons in the forward direction, especially for the high energy electrons provided by the recollision process. This is an important feature in the context of using carbon nanotubes as future sources of collimated electron beams for time-resolved diffraction experiments.

ACKNOWLEDGMENTS:

C.-Z.G. thanks the financial support from China Scholarship Council (CSC) (No. [2013]3009). We thank Institut Universitaire de France, European ITN network CORINF and French ANR contract LASCAR (ANR-13-BS04-0007) for support during the realization of this work. It was also granted access to the HPC resources of CalMiP (Calcul en Midi-Pyrénées) under the allocation P1238, and of RRZE (Regionales Rechenzentrum Erlangen).

[1] S. Hilbert, A. Neukirch, C. Uiterwaal, and H. Batelaan, J. Phys. B: At., Mol. Opt. Phys. **42**, 141001 (2009).
[2] J. C. Williamson, J. Cao, H. Ihee, H. Frey, and A. H. Zewail, Nature **386**, 159 (1997).
[3] V. A. Lobastov, R. Srinivasan, and A. H. Zewail, Proc. Natl. Acad. Sci. U. S. A. **102**, 7069 (2005).
[4] P. M. Paul, E. S. Toma, P. Breger, G. Mullot, F. Augé, P. Balcou, H. G. Muller, and P. Agostini, Science **292**, 1689 (2001).
[5] P. Agostini and L. F. DiMauro, Rep. Prog. Phys. **67**, 813 (2004).
[6] R. Bormann, M. Gulde, A. Weismann, S. V. Yalunin, and C. Ropers, Phys. Rev. Lett. **105**, 147601 (2010).
[7] M. Schenk, M. Krüger, and P. Hommelhoff, Phys. Rev. Lett. **105**, 257601 (2010).
[8] M. Krüger, M. Schenk, P. Hommelhoff, G. Wachter, C. Lemell, and J. Burgdörfer, New J. Phys. **14**, 085019 (2012).
[9] D. L. Carroll, P. Redlich, P. M. Ajayan, J. C. Charlier, X. Blase, A. De Vita, and R. Car, Phys. Rev. Lett. **78**, 2811 (1997).
[10] Y. Saito, K. Hamaguchi, K. Hata, K. Uchida, Y. Tasaka, F. Ikazaki, M. Yumura, A. Kasuya, and Y. Nishina, Nature **389**, 554 (1997).
[11] N. Nilius, N. Ernst, and H.-J. Freund, Phys. Rev. Lett. **84**, 3994 (2000).
[12] M. Bionta, B. Chalopin, A. Masseboeuf, and B. Chatel, Ultramicroscopy (2014), in press.
[13] R. Saito, M. Fujita, G. Dresselhaus, and M. S. Dresselhaus, Phys. Rev. B **46**, 1804 (1992).
[14] Y. Kawashita, T. Nakatsukasa, and K. Yabana, J. Phys. Condens. Matter **21**, 064222 (2009).
[15] T. Fennel, K.-H. Meiwes-Broer, J. Tiggesbäumker, P. M. Dinh, P.-G. Reinhard, and E. Suraud, Rev. Mod. Phys. **82**, 1793 (2010).
[16] E. Runge and E. K. U. Gross, Phys. Rev. Lett. **52**, 997 (1984).
[17] R. M. Dreizler and E. K. U. Gross, *Density Functional Theory: An Approach to the Quantum Many-Body Problem* (Springer-Verlag, Berlin, 1990).
[18] J. P. Perdew and Y. Wang, Phys. Rev. B **45**, 13244 (1992).
[19] H. W. Kroto, J. R. Heath, S. C. O'Brien, R. F. Curl, and R. E. Smalley, Nature **318**, 162 (1985).
[20] M. J. Puska and R. M. Nieminen, Phys. Rev. A **47**, 1181 (1993).
[21] D. Bauer, F. Ceccherini, A. Macchi, and F. Cornolti, Phys. Rev. A **64**, 063203 (2001).
[22] E. Cormier, P.-A. Hervieux, R. Wiehle, B. Witzel, and H. Helm, Eur. Phys. J. D **26**, 83 (2003).
[23] P.-G. Reinhard, P. Wopperer, P. M. Dinh, and E. Suraud, in *ICQNM 2013, The Seventh International Conference on Quantum, Nano and Micro Technologies* (2013), pp. 13–17.
[24] K. Hedberg, L. Hedberg, D. S. Bethune, C. Brown, H. Dorn, R. D. Johnson, and M. De Vries, Science **254**, 410 (1991).
[25] M. E. Madjet, H. S. Chakraborty, J. M. Rost, and S. T. Manson, J. Phys. B: At., Mol. Opt. Phys. **41**, 105101 (2008).

[26] D. L. Lichtenberger, M. E. Jatcko, K. W. Nebesny, C. D. Ray, D. R. Huffman, and L. D. Lamb, Mater. Res. Soc. Symp. Proc. **206**, 673 (1990).

[27] K. Sattler, *Handbook of Nanophysics: Clusters and Fullerenes*, Handbook of Nanophysics (CRC Press, 2010).

[28] S. Korica, A. Reinköster, M. Braune, J. Viefhaus, D. Rolles, B. Langer, G. Fronzoni, D. Toffoli, M. Stener, P. Decleva, et al., Surf. Sci. **604**, 1940 (2010).

[29] D. Toffoli and P. Decleva, Phys. Rev. A **81**, 061201(R) (2010).

[30] M. Araidai, Y. Nakamura, and K. Watanabe, Phys. Rev. B **70**, 245410 (2004).

[31] J. A. Driscoll, B. Cook, S. Bubin, and K. Varga, J. Appl. Phys. **110**, 024304 (2011).

[32] P. Wopperer, P. M. Dinh, P.-G. Reinhard, and E. Suraud, Phys. Rep. **562**, 1 (2015).

[33] C.-Z. Gao, P. Wopperer, P. M. Dinh, P.-G. Reinhard, and E. Suraud, J. Phys. B: At., Mol. Opt. Phys. **48**, 105102 (2015).

[34] P. Wopperer, C. Z. Gao, T. Barillot, C. Cauchy, A. Marciniak, V. Despré, V. Loriot, G. Celep, C. Bordas, F. Lépine, et al., Phys. Rev. A **91**, 042514 (2015).

[35] G. Herink, D. Solli, M. Gulde, and C. Ropers, Nature **483**, 190 (2012).

[36] P. Wopperer, B. Faber, P. M. Dinh, P.-G. Reinhard, and E. Suraud, Phys. Lett. A **375**, 39 (2010).

[37] P. Wopperer, B. Faber, P. M. Dinh, P.-G. Reinhard, and E. Suraud, Phys. Rev. A **82**, 063416 (2010).

[38] N. W. Ashcroft and N. D. Mermin, *Solid State Physics* (Saunders College, Philadelphia, 1976).

[39] W. Ekardt, Phys. Rev. Lett. **52**, 1925 (1984).

[40] M. Brack, Rev. Mod. Phys. **65**, 677 (1993).

[41] O. Gunnarsson, H. Handschuh, P. S. Bechthold, B. Kessler, G. Ganteför, and W. Eberhardt, Phys. Rev. Lett. **74**, 1875 (1995).

[42] P.-G. Reinhard and E. Suraud, Ann. Phys. (N.Y.) **354**, 183 (2015).

[43] L. V. Keldysh, Sov. Phys. JETP **20**, 1307 (1965).

[44] E. Mevel, P. Breger, R. Trainham, G. Petite, P. Agostini, A. Migus, J.-P. Chambaret, and A. Antonetti, Phys. Rev. Lett. **70**, 406 (1993).

[45] H. Li, B. Mignolet, G. Wachter, S. Skruszewicz, S. Zherebtsov, F. Süßmann, A. Kessel, S. A. Trushin, N. G. Kling, M. Kübel, et al., Phys. Rev. Lett. **114**, 123004 (2015).

[46] F. Calvayrac, P.-G. Reinhard, E. Suraud, and C. A. Ullrich, Phys. Rep. **337**, 493 (2000).

[47] P.-G. Reinhard and E. Suraud, *Introduction to Cluster Dynamics* (Wiley, New York, 2003).

[48] P.-G. Reinhard and R. Y. Cusson, Nucl. Phys. A **378**, 418 (1982).

[49] M. D. Feit, J. A. Fleck, and A. Steiger, J. Comp. Phys. **47**, 412 (1982).

[50] F. Calvayrac, E. Suraud, and P.-G. Reinhard, Ann. Phys. (N.Y.) **255**, 125 (1997).

[51] A. Pohl, P.-G. Reinhard, and E. Suraud, Phys. Rev. Lett. **84**, 5090 (2000), URL `http://link.aps.org/doi/10.1103/PhysRevLett.84.5090`.

[52] A. Pohl, P.-G. Reinhard, and E. Suraud, J. Phys. B **34**, 4969 (2001).

[53] P. M. Dinh, P. Romaniello, P.-G. Reinhard, and E. Suraud, Phys. Rev. A **87**, 032514 (2013).

[54] D. J. Park, B. Piglosiewicz, S. Schmidt, H. Kollmann, M. Mascheck, and C. Lienau, Phys. Rev. Lett. **109**, 244803 (2012).

[55] P. B. Corkum, Phys. Rev. Lett. **71**, 1994 (1993).

[56] G. G. Paulus, W. Becker, W. Nicklich, and H. Walther, J. Phys. B: At., Mol. Opt. Phys. **27**, L703 (1994).

[57] C. Cornaggia, Phys. Rev. A **78**, 041401 (2008).

[58] R. Kopold and W. Becker, J. Phys. B: At., Mol. Opt. Phys. **32**, L419 (1999).

[59] M. V. Frolov, N. L. Manakov, and A. F. Starace, Phys. Rev. A **79**, 033406 (2009).

[60] E. E. B. Campbell, K. Hansen, K. Hoffmann, G. Korn, M. Tchaplyguine, M. Wittmann, and I. V. Hertel, Phys. Rev. Lett. **84**, 2128 (2000).

[61] M. Kjellberg, O. Johansson, F. Jonsson, A. V. Bulgakov, C. Bordas, E. E. B. Campbell, and K. Hansen, Phys. Rev. A **81**, 023202 (2010).

[62] A. Pohl, P.-G. Reinhard, and E. Suraud, J. Phys. B **37**, 3301 (2004).

[63] M. Busuladžić, A. Gazibegović-Busuladžić, and D. Milošević, Laser Phys. **16**, 289 (2006).

[64] M. Krüger, M. Schenk, and P. Hommelhoff, Nature **475**, 78 (2011).

[65] M. Krüger, M. Schenk, M. Förster, and P. Hommelhoff, J. Phys. B: At., Mol. Opt. Phys. **45**, 074006 (2012).

[66] G. G. Paulus, F. Grasbon, H. Walther, R. Kopold, and W. Becker, Phys. Rev. A **64**, 021401 (2001).

[67] M. Lewenstein, P. Balcou, M. Y. Ivanov, A. L'Huillier, and P. B. Corkum, Phys. Rev. A **49**, 2117 (1994).

[68] D. Milošević, G. Paulus, D. Bauer, and W. Becker, J. Phys. B: At., Mol. Opt. Phys. **39**, R203 (2006).